Journal
American Ceramic Society

ORIGINAL ARTICLE

Revealing the solid-state processing mechanisms of antiferroelectric AgNbO$_3$ for energy storage

Mao-Hua Zhang[1] | **Leif Carstensen**[2] | **Changhao Zhao**[1] | **Lovro Fulanović**[1] | **Wolfgang Donner**[2] | **Jurij Koruza**[1]

[1]Nonmetallic Inorganic Materials, Department of Materials and Earth Sciences, Technical University of Darmstadt, Darmstadt, Germany

[2]Structure Research, Department of Materials and Earth Sciences, Technical University of Darmstadt, Darmstadt, Germany

Correspondence
Jurij Koruza, Nonmetallic Inorganic Materials, Department of Materials and Earth Sciences, Technical University of Darmstadt, Darmstadt 64287, Germany.
Email: koruza@ceramics.tu-darmstadt.de

Abstract

AgNbO$_3$ is one of the prominent lead-free antiferroelectric (AFE) oxides, which readily exhibits a field-induced AFE to ferroelectric phase transition and thus a high energy storage density. The solid-state synthesis of AgNbO$_3$ is considered difficult and an oxidizing atmosphere is typically employed during AgNbO$_3$ processing, on the premise that oxygen can prevent possible decomposition of the silver oxide at high temperatures. However, details about the influence of processing parameters on the functional properties of AFE AgNbO$_3$ are insufficiently understood. In this work, the solid-state reaction of a stoichiometric AgO and Nb$_2$O$_5$ mixture was investigated. We found that ball milling can convert AgO into metallic Ag, which is beneficial for lowering the reaction temperature for the formation of the perovskite phase to 500–600℃. Moreover, the influence of the processing atmosphere (air, O$_2$, and N$_2$) was investigated by thermal analysis and *in situ* X-ray diffraction. Since the reaction between Ag and Nb$_2$O$_5$ to form AgNbO$_3$ requires oxygen uptake, AgNbO$_3$ was only found to form in air and O$_2$, whereby the kinetics were faster in the latter case. All the sintered AgNbO$_3$ samples exhibited a similar crystallographic structure, although the samples processed in O$_2$ had a lower oxygen vacancy concentration. Despite this, well-defined AFE double polarization loops were obtained in all cases. Our results indicate that decomposition of sliver oxide during ball milling is beneficial for the solid-state reaction, while a pure O$_2$ atmosphere is not essential for the synthesis of high-quality AgNbO$_3$. These findings may simplify the processing and facilitate further research of AgNbO$_3$-based antiferroelectrics.

KEYWORDS
AgNbO$_3$, antiferroelectrics, dielectric materials/properties, energy storage, *in situ* XRD, phase transition, solid-state reaction, X-ray methods

1 | INTRODUCTION

Antiferroelectric (AFE) oxides are recently drawing increased attention due to their potential application in the realm of energy storage[1,2] and caloric cooling.[3,4] Their key feature is the unique electric-field (*E*-field)-induced AFE to ferroelectric (FE) phase transition, which is accompanied by a rapid polarization and strain increase upon *E*-field application and a release of polarization charges when the *E*-field is removed.

Perovskite niobates $AgNbO_3$ (AN) and $NaNbO_3$ (NN) are the most widely studied lead-free AFE compounds and represent the basis for a number of solid solutions with very high energy storage densities.[5–10] They both possess a complex sequence of temperature-induced phase transitions.[11–13] Early papers reported that the powder diffraction pattern of $AgNbO_3$ resembles that of $NaNbO_3$ at room temperature (RT) and the structures of the two compounds were regarded as isomorphous.[14,15] However, although the virgin AFE states (i.e., prior to the application of *E*-field) of AN and NN exhibit the *Pbcm* space group, they are slightly different in their octahedral tilt systems, which are $(a^-b^-c^-)/(a^-b^-c^+)$ and $(a^-a^-b^-)$ / $(a^-a^-b^+)$ for AN[16] and NN,[17] respectively. A subsequent close inspection of the diffraction patterns also exposed different superlattice reflections.[18] Despite the similar structures, AN and NN can be easily distinguished when exposed to large *E*-fields: while the *E*-field-induced phase transition behavior is irreversible in NN,[19–22] AN readily reveals double polarization hysteresis loops that are characteristic of reversible transitions.[23,24] Due to this, AN generally exhibits a higher energy storage density. For example, undoped AN ceramics has a recoverable energy storage density of 1.6–2.1 J/cm^3,[5,25,26] with an efficiency of 40%.[5] Unmodified NN ceramics exhibit a storage density of 0.12 J/cm^3, while increased storage density has been reported for compositions modified with $SrSnO_3$ (0.90 J/cm^3 with an efficiency of 21% at 17 kV/mm),[10] $CaZrO_3$ (0.55 J/cm^3 with an efficiency of 63% at 13 kV/mm),[26] and $Bi_{1/2}Na_{1/2}TiO_3$ (12.2 J/cm^3 with an efficiency of 69% at 68 kV/mm).[9]

Early researchers pointed out that processing of AN in air atmosphere results in poor-quality dark ceramic samples with metallic silver precipitates.[27] Thermal decomposition of AgO in air was investigated in the 1980s,[28,29] as the material was considered for cathodes used in silver oxide/zinc batteries. It was reported that AgO decomposes into intermediate silver oxide products between 100 and 400℃ (first to Ag_2O_3/Ag_2O mixture and later to Ag_2O), and then into metallic silver above 400℃. This led to the general view that the difficulty in AN processing is related to the thermodynamic instability of silver oxide (AgO or Ag_2O). Hence, oxygen atmosphere is typically employed during processing to prevent possible decomposition of the silver oxide at high temperatures,[5,14,24,25,30] given the
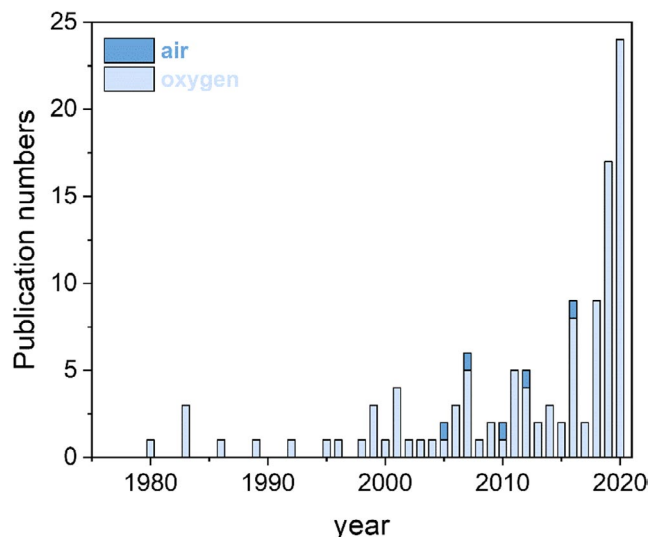

FIGURE 1 Publications on $AgNbO_3$ using air atmosphere (dark blue) and oxygen atmosphere (light blue) in the time period from 1980 to 2020. Dark blue color indicates the following papers: (1) Saito et al. in 2005,[31] (2) Valant et al. in 2007,[32] (3) Nautiyal et al. in 2010,[33] (4) Sydorchuk et al. in 2013,[34] and (5) Li et al. in 2016[35]

concern that decomposition would introduce defects into the ceramics and deteriorate the sample quality.[25] Out of more than 120 publications published on AN from 1980 to 2020, only five reported processing in air atmosphere, while others used pure oxygen (Figure 1).

However, the results presented in the few publications reporting air processing are appealing. For example, Valant et al. demonstrated that $AgNbO_3$ could be successfully obtained in air using either metallic Ag powder or Ag_2O as the silver source.[32] In the latter case, the starting Ag_2O was found to first reduce to metallic Ag, which further reacted with O_2 and Nb_2O_5 to form the perovskite phase. The reaction kinetic was controlled by oxygen diffusion. Other authors reported achieving phase-pure $(Ag, Li)NbO_3$,[31] $AgNbO_3$,[33, 34] and $Ag(Nb, Ta)O_3$.[35] The above results suggest that the use of pure oxygen atmosphere during the processing of AN may be redundant. AN processing in air would represent an important practical and economic benefit. However, the above studies focused on investigating the dielectric and photocatalytic properties, while field-induced AFE to FE transitions were not reported.

In this work, solid-state synthesis and sintering of $AgNbO_3$ were conducted in air, O_2, and N_2. Thermogravimetric analysis (TGA), differential thermal analysis (DTA), and *in situ* high temperature X-ray diffraction were performed on stoichiometric AgO/Nb_2O_5 powder mixtures to follow the reactions, while structural, microstructural and electrical measurements were carried out on sintered ceramic pellets. The results reveal that dense AN pellets with excellent AFE properties can be obtained by processing in air atmosphere.

2 | EXPERIMENTAL WORK

$AgNbO_3$ ceramics were synthesized using the solid-state route. High-purity powders of AgO (99.90%; Alfa Aesar) and orthorhombic Nb_2O_5 (99.99%; Sinopharm) were stoichiometrically weighed, mixed, and milled in a planetary ball mill using yttria-stabilized zirconia balls in ethanol at 250 rpm for 16 h. The material of ball-milling jar was cast polyamide 6, also referred to as nylon type 6 (PA6G). The powder mixture was subsequently dried and calcined either in air or pure oxygen (purity 99.998%) atmospheres at 850℃ for 6 h in a tube furnace (ROC75/450/16; Thermoconcept). The as-calcined powder obtained in both atmospheres was yellowish in color and was subsequently ball milled at 250 rpm for 16 h, dried, and compacted into disks with 10 mm in diameter and 1.5 mm in thickness. The color of the as-calcined powder turned to gray after ball milling. The discs were subject to cold isostatic pressing with 200 MPa. Sintering was done at 1080℃ for 3 h in either air or oxygen atmospheres in the same tube furnace. The samples are labeled according to their calcination and sintering atmospheres. For example, "air–O_2" refers to a sample that was calcined in air and sintered in O_2 atmosphere. Four different samples, that is, air–air, air–O_2, O_2–air, and O_2–O_2 are presented in the following. The density of the sintered samples was determined by the Archimedes method.

Thermogravimetric analysis and DTA were performed using a simultaneous TGA/DTA thermal analyzer (STA 449C Jupiter; Netzsch) with Fourier Transform Infrared Spectrometer (Bruker Tensor 27, Mid-infrared range with gas cell; Bruker Optics) for evolved gas analysis. Heating rate was 5℃/min. The thermal analysis of AgO was conducted in air and O_2 atmospheres, while the analysis of the homogenized stoichiometric mixture of raw chemicals AgO and Nb_2O_5 was conducted in air, O_2 and N_2 atmospheres. Gases with technical purity were used, whereby the synthetic air had a mixture of 80% N_2 and 20% O_2.

The *in situ* high-temperature X-ray diffraction (XRD) measurements were conducted on a laboratory diffractometer (Bruker D8) with high-temperature chamber (HTK-1200N; Anton Paar) and Cu Kα radiation. The XRD patterns were collected on the same sample at 30, 100, 200, 300, 400, 500, and 600℃ in the 2θ range of 20°–80° with step size of 0.02° using the Bragg-Brentano geometry. Each pattern collection took approximately 52 min and the ramping rate between different temperatures was 5 K/min.

Scanning electron microscopy (XL 30 FEG; Philips) was used to examine the morphology of the powders and the microstructures of the sintered samples. The latter were ground, polished with diamond paste down to 1.0 μm particle size, and thermally etched at 1050℃ for 30 min. Polished sintered samples were additionally examined in the reflected polarized light mode of the Axio Imager 2 optical microscope (Zeiss).

The structure of calcined powder after ball milling was investigated using an X-ray diffractometer with Bragg-Brentano geometry (XRD, Bruker AXS D8 Advance) with Cu Kα radiation. The XRD measurement of the sintered samples was performed using a Huber G670 Guinier camera with a Huber G611 Ge (111) Johansson-monochromator in transmission mode and $CuK_{\alpha 1}$ radiation. The signal was detected using a luminescent image plate detector with a radius of 90 mm. The Rietveld refinements of the Guinier camera data were performed using a sample absorption correction as given by Berger.[36] Air absorption was handled using a cosine function for the pathlength derived from the 45° incidence angle at the sample surface. The starting parameters for the refinement were taken from the neutron data refinements of Sciau et al.[37] The refinement of structural parameters was restricted to the positions of Ag and Nb ions and the Debye-Waller factor of the oxygen ions, which was assumed to be uniform for all oxygen sites. Note that the sintered ceramic pellets were crushed into powder form and annealed at 500℃ to relax stresses before structural characterization was conducted.

The sintered disc samples for electrical characterization were ground to a thickness of 0.25 mm, followed by 400℃ stress-free annealing in air and sputtering with platinum electrodes. All the samples were electroded across entire main faces and cut to a dimension of 1.5 mm × 1.5 mm × 0.25 mm. Polarization- and strain-hysteresis loops were measured with a triangular field of 14 kV/mm at 1 Hz using a modified Sawyer-Tower circuit and an optical displacement sensor (D63; Philtec, Inc.). The hysteresis loops in the second cycle are shown. Temperature-dependent permittivity measurements at a frequency of 10 kHz were performed using an impedance analyzer (4192A LF; Hewlett-Packard).

3 | RESULTS AND DISCUSSIONS

3.1 | Solid-state reactions

Thermal analysis was first performed on the starting powder AgO, which was heated in air and O_2 (Figure 2A). Note that this compound is a mixed oxidation state silver oxide ($Ag^IAg^{III}O_2$, therefore strictly speaking Ag_2O_2).[38] In both atmospheres, thermal decomposition of AgO consists of three stages. The first stage starts at 173℃ and finishes at 203℃, accompanied by a small exothermic peak at 174℃. During this first stage, AgO decomposes as follows[29]:
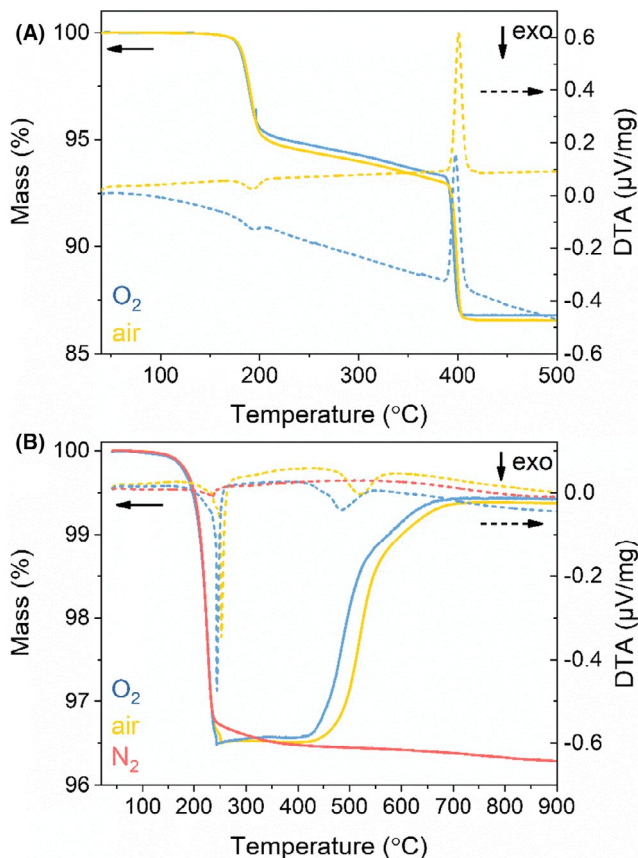
$$4AgO \rightarrow n\left(Ag_2O_3\right) + (2-n)Ag_2O + (1-n)O_2 \quad (1)$$
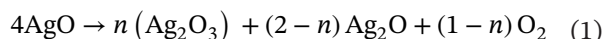
FIGURE 2 TG and DTA curves of (A) AgO decomposition in air and O_2 and (B) $AgNbO_3$ formation upon heating a milled stoichiometric mixture in air, O_2, and N_2 atmospheres. Temperatures reported in the text refer to the onset temperatures of reactions, which are defined as the intersection of the tangents of the peak with the extrapolated baseline. Please note that the different slopes of the DTA curves in (A) are related to different baselines TG, thermogravimetric; DTA, differential thermal analysis

The second stage is indicated by a slope change in the TG curve at 202°C. In this stage, Ag_2O_3 decomposes into Ag_2O before further decomposition of Ag_2O starts at 388°C. Merging the decompositions in the first and second stages, the decomposition of AgO into Ag_2O is summarized as:

$$2AgO \rightarrow Ag_2O + 1/2O_2 \qquad (2)$$
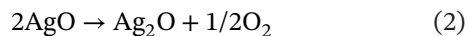
A total mass loss of 7.1% in air and 6.8% in oxygen is observed up to 388°C, which are close to the theoretically calculated loss of 6.5% from Equation (2). In the third stage, decomposition of Ag_2O into metallic Ag starts at 388°C and finishes at 404°C, accompanied by a strong endothermic peak at 394°C:

$$Ag_2O \rightarrow 2Ag + 1/2O_2 \qquad (3)$$
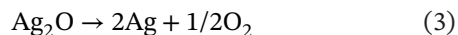
A mass loss of 6.3% in air and 6.4% in O_2 is observed in the third stage, which corresponds to the theoretically

calculated loss of 6.9% from Equation (3). These experimental results are consistent with previous decomposition studies of AgO in air atmosphere.[28,29] Moreover, they indicate that the decomposition of AgO in air is not different from the decomposition in pure O_2. This contradicts the argument that oxygen atmosphere can prevent possible decomposition of the silver oxide into metallic silver during AN synthesis at high temperatures.

In the following, *in situ* high temperature XRD and thermal analysis are employed to study the solid-state reactions during heating of the homogenized stoichiometric mixture of AgO and Nb_2O_5 (calcination process). The XRD characterization of high-energy ball milled AgO/Nb_2O_5 mixture as a function of temperature in air is shown in Figure 3. Interestingly, while the powder mixture before milling consisted of Nb_2O_5 and AgO (Figure S1), the XRD pattern of ball milled powder mixture at RT revealed a mixture of Nb_2O_5 and metallic Ag. A visual comparison of the color of the mixture before and after ball milling is shown in Figure S2. The color changes from grey before milling to dark black after milling, indicating a decomposition of AgO into metallic Ag. Mechanochemical reduction of Ag_2O into metallic Ag in a planetary ball milling has been reported before.[39] The XRD patterns remained unchanged upon heating to 400°C (Figure 3). The solid-state reaction between Ag and Nb_2O_5 occurred in the temperature range of 400–500°C, resulting in the formation of the perovskite $AgNbO_3$ phase. However, at 500°C the reaction is incomplete, as evidenced by remaining minor Nb_2O_5 and Ag reflections. These disappear at 600°C.
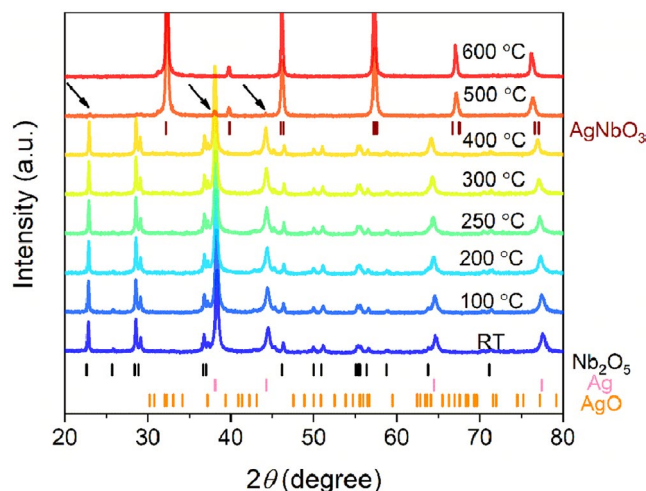

**FIGURE 3** *In situ* XRD of the ball-milled stoichiometric mixture as a function of temperature from RT to 600°C. The set of tick marks represents the reflections associated with the structures of AgO, Ag, Nb_2O_5, and $AgNbO_3$ (for labels, please refer to the PDF-ICDD database, 2011). Unreacted Ag and Nb_2O_5 at 500°C are highlighted by black arrows. RT, room temperature; XRD, X-ray diffraction

The XRD results were complemented by thermal analysis of the ball milled mixture. The average particle size of the mixture was 2.01 μm (distribution is shown in Figure S3). TG and DTA curves recorded in air and O_2 show strong similarities, while a clear difference is evident for the curve measured in N_2 (Figure 2B). Between 198 and 244°C, a mass loss of 3.5%, 3.5%, and 3.2% was observed in air, O_2, and N_2 atmospheres, respectively, accompanied by a strong exothermic peak in air and O_2 atmospheres and a less significant one in N_2 atmosphere. Evolved gas analysis (Figure S4) revealed that this mass loss is related to a release of gaseous acetic acid ($C_2H_4O_2$), carbon dioxide (CO_2), and carbon monoxide (CO). These are likely to originate either from the reaction of ethanol (milling medium) with the mechanochemically-released O_2, additionally catalyzed by the presence of metallic Ag, or from nylon pollutants introduced to the powder mixture during ball milling, which then decompose on heating.

The mass loss is followed by a mass gain above 400°C, which is absent in N_2 atmosphere. The mass gain signifies the start of the solid-state reaction and formation of $AgNbO_3$, in agreement with the high temperature XRD results (Figure 3). The reaction onset is at 418 and 457°C in O_2 and air atmospheres, respectively. A mass gain of 3.0% and 2.9% is observed in O_2 and air when the reaction completes at 656 and 680°C, respectively. The observed mass gain is due to O_2 uptake and corresponds to a theoretically calculated gain of 3.3% from the reaction:

$$2Ag + Nb_2O_5 + 1/2O_2 \rightarrow 2AgNbO_3 \qquad (4)$$
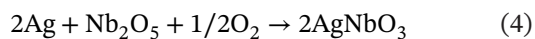
The reaction is accompanied by a small exothermic peak. Note that the reaction finishes at a lower temperature in O_2, indicating faster formation kinetics related to a higher oxygen partial pressure. This result confirms the reaction control by oxygen diffusion, as reported by Valant et al.[32] In contrast, the flat mass loss curve and absence of a DTA peak indicate that no $AgNbO_3$ formation occurs in N_2.

The benefit of high-energy ball milling for $AgNbO_3$ formation was additionally demonstrated by high-temperature XRD analysis of an unmilled stoichiometric powder mixture of AgO and Nb_2O_5 (Figure S5). Unlike for the milled powder, heating of the unmilled powder resulted in large amounts of unreacted Ag and Nb_2O_5 even at 600°C.

3.2 | Structural characterization

XRD patterns of both air-calcined and O_2-calcined powders exhibit a typical orthorhombic perovskite structure (Figure 4A). Both powders show a similar particle
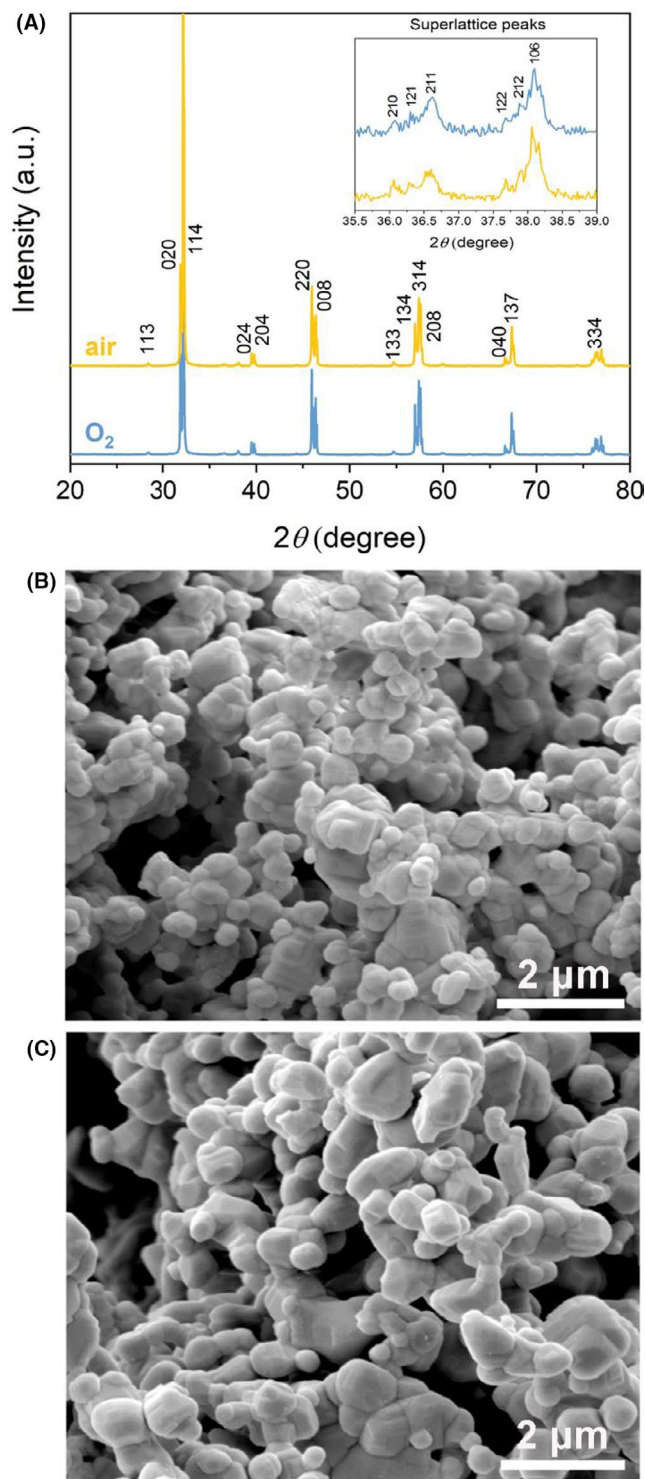

FIGURE 4 (A) XRD patterns of ball-milled stoichiometric AgO/Nb_2O_5 powder mixture after calcination in O_2 and air atmospheres. A zoom-in of superlattice peaks is shown in the inset. Morphology of the calcined powder prepared in (B) air and (C) O_2 atmospheres after heated to 900°C without subsequent ball milling. XRD, X-ray diffraction

morphology (Figure 4B,C). However, the average particle size of the O_2-calcined powder is slightly larger, which is related to the faster formation kinetics (Figure 2B).

Powder compacts of the two calcined powders were sintered at 1080℃ in air and O_2 atmospheres and, hence, four different samples, abbreviated as air–air, air–O_2, O_2–air, and O_2–O_2, were obtained. Note that the sintering temperature is well below the reported AN decomposition temperature of 1124℃.[32] The samples exhibit a high relative density of 97.2%–99.4%, as listed in Table 1. Sintered samples were polished and examined using optical microscopy. All samples exhibit similar bimodal grain size distributions and abnormal grain growth (Figure S6), which was previously reported for AN samples[24] and other niobates.[40] Please note that in order to compare only the influence of the sintering atmospheres, the sintering temperature and time were fixed and not optimized in the present work. Minor inclusions were identified in all sintered samples (Figures S7 and S8). The brighter contrast indicated that the inclusions are Ag-rich (Figure S9) and could represent residues of the metallic silver from the intermediate reaction stage (Equation 4; Figure 2B). Valant et al. also reported the presence of metallic silver after synthesis, although the XRD analysis suggested a single phase state.[32] Nevertheless, the amount of these inclusions is relatively small and is similar in all four samples. Overall, we can conclude that the microstructural parameters, i.e., density, grain distributions, and the existence of Ag-rich inclusions are not influenced by the processing atmospheres used in this study. For completeness, the AgO/Nb_2O_5 powder mixture was also calcined and sintered in N_2 atmosphere, which resulted in the appearance of large metallic silver drops on the surfaces of the sintered samples (Figure S10). The XRD pattern of a ball-milled AgO/Nb_2O_5 powder after calcination in N_2 is shown in Figure S11, which consists of a mixture of metallic Ag and Nb_2O_5.

To investigate the influence of the sintering atmosphere on the crystallographic structure, two sintered samples (air–air and O_2–O_2) were further analyzed by the Rietveld refinement of the XRD data. Please note that the identification of the correct space group of $AgNbO_3$ at RT is non-trivial, as diffractograms can generally be well-described by both non-polar *Pbcm* and polar *Pmc2$_1$* models.[7,41] This is evidenced by the very close peak positions of the two space groups shown in the inset of Figure 5. In our work, the peak positions of the investigated samples are

TABLE 1 Densities of the $AgNbO_3$ samples calcined and sintered in different atmospheres

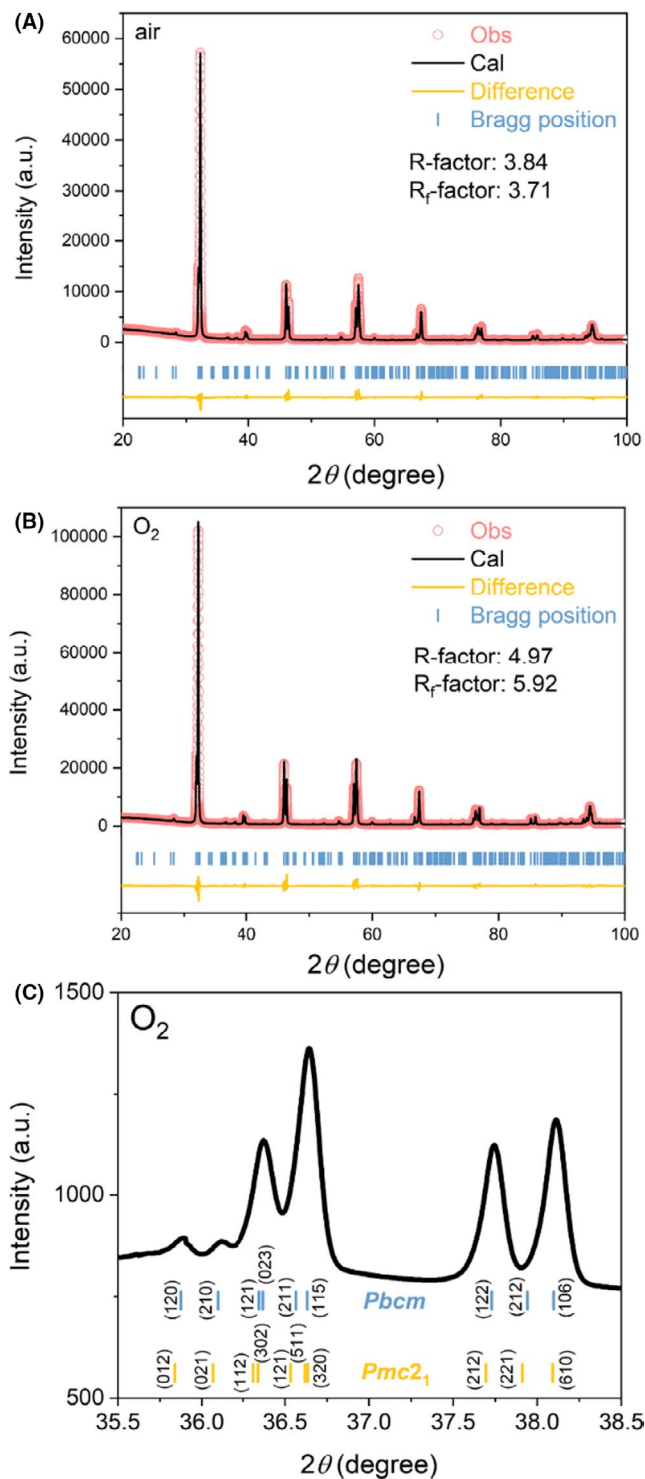| Sample	Density (g/cm³)	Relative density (%)
Air–air	6.68	98.3
Air–O_2	6.76	99.4
O_2–air	6.67	98.1
O_2–O_2	6.61	97.2

FIGURE 5 Rietveld refinements of XRD patterns of (A) air-sintered and (B) O_2-sintered $AgNbO_3$ using the *Pbcm* model. (C) Enlarged view of the superlattice peaks in the 2θ range of 35.5°–40.5°. The set of tick marks represents the reflections associated with the *Pbcm* (blue) and *Pmc2$_1$* (yellow) space groups. XRD, X-ray diffraction

more consistent with the reflections associated with the *Pbcm* model, which also agrees to the expected non-polar nature of the virgin samples. The results of the Rietveld

TABLE 2 Refined structural parameters of the air-sintered (air–air) and O$_2$-sintered (O$_2$–O$_2$) samples

	O$_2$–O$_2$	Air–air
a [Å]	5.5466(3)	5.5451(9)
b [Å]	5.6024(2)	5.5994(7)
c [Å]	15.6404(9)	15.6421(1)
Unit cell volume [Å^3]	486.022(7)	485.689(9)
$x(Ag_1)$	−0.255(7)	−0.253(5)
$y(Ag_1)$	0.25	0.25
$z(Ag_1)$	0	0
$x(Ag_2)$	−0.255(7)	−0.252(5)
$y(Ag_2)$	0.230(3)	0.233(3)
$z(Ag_2)$	0.25	0.25
$x(Nb)$	0.244(7)	0.240(3)
$y(Nb)$	0.224(2)	0.224(2)
$z(Nb)$	0.125(2)	0.124(2)
$B_{iso}(O)$	1.05(5)	1.2(1)
R-factor	4.97	3.84
R_f-factor	5.92	3.71

refinements are given in Figure 5C, while the fitted lattice constants of the air-sintered and O$_2$-sintered samples are shown in Table 2. The differences in the lattice parameters are negligible. Slight differences in the coordinates of Ag(1), Ag(2) and Nb ions were identified, which are expected to be related to the slightly different lattice distortions within the orthorhombic *ab* plane, as discussed in the next section. The isotropic displacement parameter B_{iso} (O) for all oxygen ions is higher for air-sintered sample than that of the O$_2$-sintered sample. Here, the B_{iso} (O) value could be interpreted as a sum of thermal and static Debye-Waller factors. The slightly higher Debye-Waller factor for the air-sintered sample may be interpreted as a sign for increased disorder at the oxygen site. The static disorder is assumed to result from a higher oxygen vacancy concentration in the air-sintered sample.

3.3 | Electrical properties

Temperature-dependent dielectric permittivity and dielectric loss of the four AgNbO$_3$ samples calcined and sintered in different atmospheres are given in Figure 6. All samples reveal very similar behavior, which is consistent with previous reports.[5,11,23,24,42] Upon heating, the phase transitions of AgNbO$_3$ follow the sequence[11,12,43]: M$_1$ → M$_2$ → M$_3$ → O$_1$ → O$_2$ → T → C, where M$_1$, M$_2$, and M$_3$ phases possess orthorhombic symmetry in rhombic orientation, while O$_1$ and O$_2$ possess orthorhombic symmetry in parallel orientation.[12] In the parallel orientation
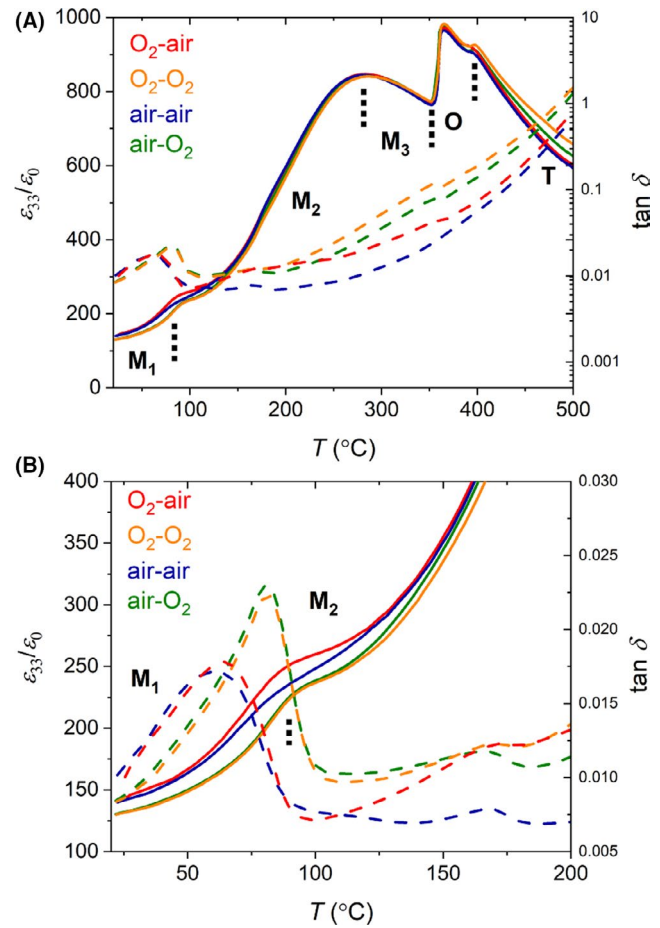
FIGURE 6 Temperature-dependent dielectric permittivity and dielectric loss (dashed lines) for the four different AgNbO$_3$ samples (A) measured up to 500℃ at 10 kHz and (B) a zoom-in on the M$_1$–M$_2$ transitions in the temperature range from room temperature to 200℃. Dashed lines indicate phase transitions. Phase transition temperatures are defined as the intersection of the tangent lines

the orthorhombic axes are parallel to the pseudocubic directions, whereas in the case of rhombic orientation the orthorhombic *a*- and *b*-axes are parallel to diagonals contained inside the faces of the same pseudocubic axis.[44] The phases T and C are tetragonal and cubic, respectively. In the permittivity curves, the phase transitions M$_2$ → M$_3$, M$_3$ → O, and O → T are observed at 287, 353, and 398℃, respectively, for all the samples, irrespective of the sintering atmosphere. Interestingly, the M$_1$ → M$_2$ transition is shifted to 86℃ for air-sintered sample, as compared to 91℃ observed in the O$_2$-sintered sample. The dielectric losses at RT are comparable, albeit slightly lower for the O$_2$-sintered samples (Table 3), which could indicate a lower concentration of oxygen vacancies expected for the O$_2$-sintered sample. The M$_1$, M$_2$, and M$_3$ phases are structurally very close to each other with only slight modifications.[45] Early researchers postulated that the presence of the diffuse phase transition (M$_1$ → M$_2$ → M$_3$) is related to the disorder of Nb

TABLE 3 Dielectric and antiferroelectric properties of the four different AgNbO₃ samples

	Air–air	Air–O₂	O₂–air	O₂–O₂
$\varepsilon_{33}/\varepsilon_0$	142	132	144	132
$\tan\delta$	0.010	0.009	0.012	0.006
P_{max} (μC/cm²)	36.9	38.4	36.9	39.5
P_r (μC/cm²)	6.4	6.5	5.3	11.3
S_{max} (%)	0.61	0.69	0.56	0.55
W_{rec} (J/cm³)	1.54	1.58	1.49	1.34
η (%)	38	36	37	29

Note: Dielectric properties $\varepsilon_{33}/\varepsilon_0$ and $\tan\delta$ were measured at 30℃ and 10 kHz. Maximum polarization P_{max}, remanent polarization P_r, recoverable energy storage density W_{rec} and efficiency η were obtained from the polarization hysteresis loops in the second cycle. Maximum strain S_{max} was obtained from the strain hysteresis loop in the first cycle.
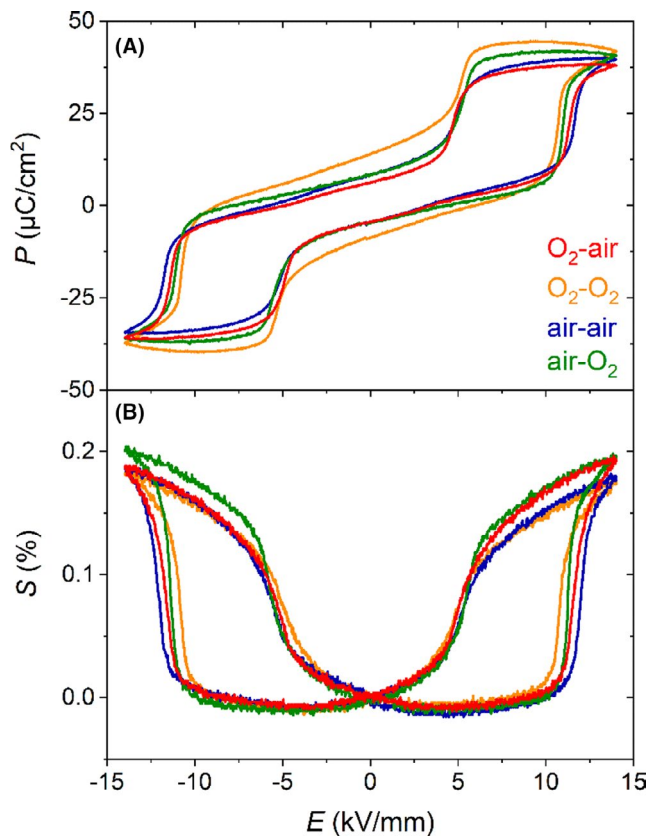

FIGURE 7 (A) Polarization and (B) strain hysteresis loops of AgNbO₃ samples under an electric field of 14 kV/mm (1 Hz, second cycle). The polarization and strain hysteresis loops obtained during the first cycle (the virgin state) are shown in Figure S12

ion displacements.[46,47] This hypothesis was validated by a subsequent study, which showed that the three M phases share the same long-range average structure with minor difference in the amplitude of atomic displacements.[44] The slightly higher M₁ → M₂ phase transition temperature of

the O₂-sintered sample, compared to the air-sintered sample, indicates a slightly higher lattice distortion for the O₂-sintered sample. As shown in Table 2, the coordinates of Ag(1)/Ag(2) and Nb are marginally different for the O₂-sintered and air-sintered samples, which is expected to result in different lattice distortions within the orthorhombic *ab* plane. The orthorhombic lattice constant ratio b/a is 1.0101 and 1.0098 for the O₂-sintered and air-sintered samples, respectively. The larger lattice distortion of the O₂-sintered sample supports the observed dielectric behavior.

Finally, all the AgNbO₃ samples were subjected to a large *E*-field of 14 kV/mm and their bipolar polarization, *P(E)*, and strain, *S(E)*, hysteresis loops are shown in Figure 7A,B, respectively. Double polarization hysteresis loops are observed for all samples. The O₂-sintered samples exhibit slightly higher polarization, which could be related to a leakage current contribution. The *S(E)* loops confirm the absence of significant differences between the samples. In summary, these large-signal data reveal that all samples exhibit well-defined AFE polarization loops, irrespective of the processing atmosphere.

4 | CONCLUSIONS

We investigated the individual steps during solid-state processing of the AFE AgNbO₃. Decomposition of AgO into metallic Ag was found to occur during high-energy ball milling. Since different milling technologies and conditions were used throughout the existing literature, this phenomenon is likely to be the origin of reported inconsistency in sample quality. The solid-state reaction between metallic Ag and Nb₂O₅ to synthesize AgNbO₃ was found to occur in the temperature range between 400 and 700℃ in both O₂ and air atmospheres, while the reaction was not possible in N₂. The reaction kinetics was slightly faster in O₂, but detailed structural analysis of the samples revealed no significant differences in the products. All sintered samples exhibited low dielectric losses and double polarization hysteresis loops, characteristic of reversible AFE to FE phase transition. The small difference in the M₁–M₂ phase transition temperatures was related to the slightly higher concentration of oxygen vacancies in the air-sintered sample. The latter also exhibited a slightly higher Debye-Waller factor, which is characteristic for increased disorder at the oxygen site. Moreover, marginally larger lattice distortion within the orthorhombic *ab* plane was identified for the O₂-sintered samples. We conclude that O₂ atmosphere is not necessary for the processing of high-quality AgNbO₃ ceramic samples with good AFE properties, but high-energy milling is desirable. These results could simplify the processing and facilitate the development of new compositions based on this material system.

ORCID

Mao-Hua Zhang https://orcid.org/0000-0002-9823-4547
Jurij Koruza https://orcid.org/0000-0002-0258-6709

REFERENCES

1. Randall CA, Fan Z, Reaney I, Chen L-Q, Trolier-McKinstry S. Antiferroelectrics: history, fundamentals, crystal chemistry, crystal structures, size effects, and applications. J Am Ceram Soc. 2021;104(8):3775–810.
2. Liu Z, Lu T, Ye J, Wang G, Dong X, Withers R, et al. Antiferroelectrics for energy storage applications: a review. Adv Mater Technol. 2018;3:1800111.
3. Geng W, Liu Y, Meng X, Bellaiche L, Scott JF, Dkhil B, et al. Giant negative electrocaloric effect in antiferroelectric La-doped $Pb(ZrTi)O_3$ thin films near room temperature. Adv Mater. 2015;27(20):3165–9.
4. Novak N, Weyland F, Patel S, Guo H, Tan X, Rödel J, et al. Interplay of conventional with inverse electrocaloric response in $(Pb, Nb)(Zr, Sn, T_i)O_3$ antiferroelectric materials. Phys Rev B. 2018;97:094113.
5. Zhao L, Liu Q, Gao J, Zhang SJ, Li JF. Lead-free antiferroelectric silver niobate tantalate with high energy storage performance. Adv Mater. 2017;29:1701824.
6. Yang D, Gao J, Shu L, Liu Y-X, Yu J, Zhang Y, et al. Lead-free antiferroelectric niobates $AgNbO_3$ and $NaNbO_3$ for energy storage applications. J Mater Chem A. 2020;8(45):23724–37.
7. Tian Y, Jin L, Hu Q, Yu K, Zhuang Y, Viola G, et al. Phase transitions in tantalum-modified silver niobate ceramics for high power energy storage. J Mater Chem A. 2019;7(2):834–42.
8. Luo N, Han K, Cabral MJ, Liao X, Zhang S, Liao C, et al. Constructing phase boundary in $AgNbO_3$ antiferroelectrics: pathway simultaneously achieving high energy density and efficiency. Nat Commun. 2020;11:4824.
9. Qi H, Zuo R, Xie A, Tian A, Fu J, Zhang Y, et al. Ultrahigh energy-storage density in $NaNbO_3$-based lead-free relaxor antiferroelectric ceramics with nanoscale domains. Adv Funct Mater. 2019;29:1903877.
10. Zhang M-H, Hadaeghi N, Egert S, Ding H, Zhang H, Groszewicz PB, et al. Design of new lead-free antiferroelectric $(1-x)NaNbO_3$-$xSrSnO_3$ compositions guided by first-principles calculations. Chem Mater. 2021;33(1):266–74.
11. Łukaszewski M, Pawełczyk M, Haňderek J, Kania A. On the phase transitions in silver niobate $AgNbO_3$. Phase Transit. 1983;3(3):247–57.
12. Kania A. An additional phase transition in silver niobate $AgNbO_3$. Ferroelectrics. 1998;205(1):19–28.
13. Megaw HD. The seven phases of sodium niobate. Ferroelectrics. 1974;7(1):87–9.
14. Francombe MH, Lewis B. Structural and electrical properties of silver niobate and silver tantalate. Acta Crystallogr. 1958;11(3):175–8.
15. Reisman A, Holtzberg F. Heterogeneous equilibria in the systems Li_2O-, Ag_2O-Nb_2O_5 and oxide-models. J Am Chem Soc. 1958;80(24):6503–7.
16. Levin I, Krayzman V, Woicik JC, Karapetrova J, Proffen T, Tucker MG, et al. Structural changes underlying the diffuse dielectric response in $AgNbO_3$. Phys Rev B. 2009;79:104113.
17. Johnston KE, Tang CC, Parker JE, Knight KS, Lightfoot P, Ashbrook SE. The polar phase of $NaNbO_3$: a combined study by powder diffraction, solid-state NMR, and first-principles calculations. J Am Chem Soc. 2010;132(25):8732–46.
18. Darlington CNW. An X-ray diffraction study of $AgNbO_3$ and comparison with $NaNbO_3$. Powder Diffr. 1999;14(4):253–7.
19. Zhelnova OA, Fesenko OE. Phase transitions and twinning in $NaNbO_3$ crystals. Ferroelectrics. 1987;75(1):469–75.
20. Ulinzheev AV, Leiderman AV, Smotrakov VG, Topolov VY, Fesenko OE. Phase transitions induced in $NaNbO_3$ crystals by varying the direction of an external electric field. Phys Solid State. 1997;39(6):972–4.
21. Zhang M-H, Fulanović L, Egert S, Ding H, Groszewicz PB, Kleebe H-J, et al. Electric-field-induced antiferroelectric to ferroelectric phase transition in polycrystalline $NaNbO_3$. Acta Mater. 2020;200:127–35.
22. Zhang M-H, Zhao C, Fulanović L, Rödel J, Novak N, Schökel A, et al. Revealing the mechanism of electric-field-induced phase transition in antiferroelectric $NaNbO_3$ by in situ high-energy x-ray diffraction. Appl Phys Lett. 2021;118:132903.
23. Fu D, Endo M, Taniguchi H, Taniyama T, Itoh M. $AgNbO_3$: a lead-free material with large polarization and electromechanical response. Appl Phys Lett. 2007;90:252907.
24. Gao J, Zhao L, Liu Q, Wang XP, Zhang SJ, Li JF. Antiferroelectric-ferroelectric phase transition in lead-free $AgNbO_3$ ceramics for energy storage applications. J Am Ceram Soc. 2018;101(12):5443–50.
25. Tian Y, Jin L, Zhang HF, Xu Z, Wei XY, Politova ED, et al. High energy density in silver niobate ceramics. J Mater Chem A. 2016;4(44):17279–87.
26. Liu Z, Lu J, Mao Y, Ren P, Fan H. Energy storage properties of $NaNbO_3$-$CaZrO_3$ ceramics with coexistence of ferroelectric and antiferroelectric phases. J Eur Ceram Soc. 2018;38(15):4939–45.
27. Kania A. $AgNb_{1-x}Ta_xO_3$ solid solutions-dielectric properties and phase transitions. Phase Transit. 1983;3(2):131–9.
28. Parkhurst WA, Dallek S, Larrick BF. Thermogravimetry-evolved gas analysis of silver oxide cathode material. J Electrochem Soc. 1984;131(8):1739–42.
29. Dallek S, West WA, Larrick BF. Decomposition kinetics of AgO cathode material by thermogravimetry. J Electrochem Soc. 1986;133(12):2451–4.
30. Kania A, Roleder K, Łukaszewski M. The ferroelectric phase in $AgNbO_3$. Ferroelectrics. 1983;52(1):265–9.
31. Saito A, Uraki S, Kakemoto H, Tsurumi T, Wada S. Growth of lithium doped silver niobate single crystals and their piezoelectric properties. Mater Sci Eng B. 2005;120(1–3):166–9.
32. Valant M, Axelsson A-K, Zou B, Alford N. Oxygen transport during formation and decomposition of $AgNbO_3$ and $AgTaO_3$. J Mater Res. 2007;22(6):1650–5.

33. Nautiyal OP, Bhatt SC, Bartwal KS. Investigations on the effect of preparation conditions on $AgNbO_3$ ceramics. J Alloy Compd. 2010;505(1):168–71.

34. Sydorchuk V, Khalameida S, Skubiszewska-Zięba J, Leboda R, Starchevskii V, Zazhigalov V, et al. Synthesis and photocatalytic properties of silver niobate [Текст]. In: Pogrebnjak A, editor. Nanomaterials: Applications & Properties (NAP-2013): 2-nd International Conference, Alushta, the Crimea. Vol. 2, 1st ed. Sumy: Sumy State University; 2013. 01PCSI12.

35. Li L, Spreitzer M, Suvorov D. The microstructure, dielectric abnormalities, polar order and microwave dielectric properties of $Ag(Nb_{1-x}Ta_x)O_3$ (x=0-0.8) ceramics. J Eur Ceram Soc. 2016;36(14):3347–54.

36. Berger SV, Boeri E, Bonnichsen RK, Sörensen JS, Sörensen NA. The crystal structure of boron oxide. Acta Chem Scand. 1953;7(4):611–22.

37. Sciau P, Kania A, Dkhil B, Suard E, Ratuszna A. Structural investigation of $AgNbO_3$ phases using x-ray and neutron diffraction. J Phys Condens Matter. 2004;16(16):2795–810.

38. Tudela D. Silver(II) oxide or silver(I,III) oxide? J Chem Educ. 2008;85(6):863.

39. Khayati GR, Janghorban K. The nanostructure evolution of Ag powder synthesized by high energy ball milling. Adv Powder Tech. 2012;23(3):393–7.

40. Koruza J, Malič B, Kosec M. Microstructure evolution during sintering of sodium niobate. J Am Ceram Soc. 2011;94(12):4174–8.

41. Fabry J, Zikmund Z, Kania A, Petříček V. Silver niobium trioxide, $AgNbO_3$. Acta Crystallogr C. 2000;56(8):916–8.

42. Tian Y, Jin L, Zhang HF, Xu Z, Wei XY, Viola G, et al. Phase transitions in bismuth-modified silver niobate ceramics for high power energy storage. J Mater Chem A. 2017;5(33):17525–31.

43. Pawełczyk M. Phase transitions in $AgTa_xNb_{1-x}O_3$ solid solutions. Phase Transit. 1987;8(4):273–92.

44. Sciau P, Kania A, Dkhil B, Suard E, Ratuszna A. Structural investigation of $AgNbO_3$ phases using x-ray and neutron diffraction. J Phys Condens Matter. 2004;16(16):2795–810.

45. Kania A. Dielectric properties of $Ag_{1-x}A_xNbO_3$ (A: K, Na and Li) and $AgNb_{1-x}Ta_xO_3$ solid solutions in the vicinity of diffuse phase transitions. J Phys D Appl Phys. 2001;34(10):1447–55.

46. Hafid M, Kugel GE, Kania A, Roleder K, Fontana MD. Study of the phase transition sequence of mixed silver tantalate-niobate $(AgTa_{1-x}Nb_xO_3)$ by inelastic light scattering. J Phys Condens Matter. 1992;4(9):2333–45.

47. Volkov AA, Gorshunov BP, Komandin G, Fortin W, Kugel GE, Kania A, et al. High-frequency dielectric spectra of $AgTaO_3$-$AgNbO_3$ mixed ceramics. J Phys Condens Matter. 1995;7(4):785–93.

SUPPORTING INFORMATION

Additional supporting information may be found online in the Supporting Information section.